




Topological electronic structure evolution with symmetry-breaking spin reorientation in $(\text{Fe}_{1-x}\text{Co}_x)\text{Sn}$

Robert G. Moore ^{1,*}, Satoshi Okamoto,¹ Haoxiang Li,¹ William R. Meier ¹, Hu Miao,¹ Ho Nyung Lee,¹ Makoto Hashimoto,² Donghui Lu ², Elbio Dagotto,^{1,3} Michael A. McGuire,¹ and Brian C. Sales¹

¹Materials Science and Technology Division, Oak Ridge National Laboratory, Oak Ridge, Tennessee 37831, USA

²Stanford Synchrotron Radiation Lightsource, SLAC National Accelerator Laboratory, Menlo Park, California 94025, USA

³Department of Physics and Astronomy, University of Tennessee, Knoxville, Tennessee 37996, USA



(Received 28 April 2022; revised 28 July 2022; accepted 15 September 2022; published 23 September 2022)

Topological materials hosting kagome lattices have drawn considerable attention due to the interplay between topology, magnetism, and electronic correlations. The $(\text{Fe}_{1-x}\text{Co}_x)\text{Sn}$ system not only hosts a kagome lattice but has a tunable symmetry-breaking magnetic moment with temperature and doping. In this study, angle-resolved photoemission spectroscopy and first-principles calculations are used to investigate the interplay between the topological electronic structure and varying magnetic moment from the planar to axial antiferromagnetic phases. Evidence for a theoretically predicted gap at the Dirac point is revealed in the low-temperature axial phase, but no gap opening is observed across a temperature-dependent magnetic phase transition. However, topological surface bands are observed to shift in energy as the surface magnetic moment is reduced or becomes disordered over time during experimental measurements. The shifting surface bands may preclude the determination of a temperature-dependent bulk gap, but this highlights the intricate connections between magnetism and topology with a surface/bulk dichotomy that can affect material properties and their interrogation.

DOI: [10.1103/PhysRevB.106.115141](https://doi.org/10.1103/PhysRevB.106.115141)

I. INTRODUCTION

Topological insulators and semimetals have received significant attention due to their unique linearly dispersive massless Dirac electronic bands that are topologically protected [1–4]. The breaking of symmetry by introducing magnetism into topological systems expands the exotic states that can be created, including the quantum anomalous Hall state, axionic insulating state, and chiral anomalies to name a few [5–8]. Breaking symmetry by the creation of a surface or interface also controls the interplay between magnetism and topology, such as, for example, the two-dimensional topological surface states observed in the antiferromagnetic phases of GdSbTe [9], EuSn_2As_2 [10], and MnBi_2Te_4 [10–15].

While theory predicts specific implications after the breaking of time-reversal symmetry on the topologically protected electronic states, such as the creation of a gap at the Dirac point, experimental observations are less clear. For example, there are conflicting reports on the existence [11,14,15] or absence [10,12,13] of an exchange gap in the topological states of MnBi_2Te_4 , as well as the coexistence of surface magnetism without a gap [16] and the creation of a gap only through tuning the Fermi level [17]. Hence, finding systems where the magnetism can be tuned is important for understanding and controlling emergent behavior in topological systems and delineating the different effects in the bulk and on the surface.

Topological materials with kagome lattices are of particular interest due to the emergence of dispersionless flat

electronic bands and saddle points, in addition to linearly dispersive bands [18–22]. In addition, magnetic kagome materials can host both ferromagnetic (FM) and antiferromagnetic (AFM) spin arrangements. For example, both Fe_3Sn_2 [19] and $\text{Co}_3\text{Sn}_2\text{S}_2$ [20] contain FM kagome lattices, while Mn_3Sn [21] displays an AFM ordering. The magnetic topological materials with kagome lattices add magnetic frustration and a large density of electronic states to systems with topological protection. It has been shown that the spin arrangement on the magnetic kagome lattice of the $(\text{Fe}_{1-x}\text{Co}_x)\text{Sn}$ system can be controlled with both composition and temperature [23]. Thus the $(\text{Fe}_{1-x}\text{Co}_x)\text{Sn}$ system provides an ideal opportunity to tune the magnetic state while observing the interplay between magnetism and topologically protected electronic states.

FeSn forms in a hexagonal structure (space group $P6/mmm$, no. 191) consisting of kagome Fe_3Sn layers separated by Sn sheets schematically shown in Fig. 1(a) [23–25]. FeSn has itinerant FM magnetic moments within the kagome lattice and parallel to the kagome plane which are aligned antiparallel with neighboring layers along the c axis to form a bulk AFM arrangement [23,25–27]. While the magnetic arrangement breaks inversion (P) and time-reversal (T) symmetry, the combination of inversion plus time-reversal (PT) symmetry is preserved along with a nonsymmorphic magnetic twofold screw rotation symmetry (S_{2z}) along the c axis [28]. Band-structure calculations including spin-orbit coupling show that the combined PT symmetry protects massless Dirac points appearing around $E - E_F \sim 0.4$ eV at the H and H' points. These Dirac points (DPs) can be viewed as a pair of degenerate Weyl-like points (WP) due to AFM coupling

*moorerg@ornl.gov

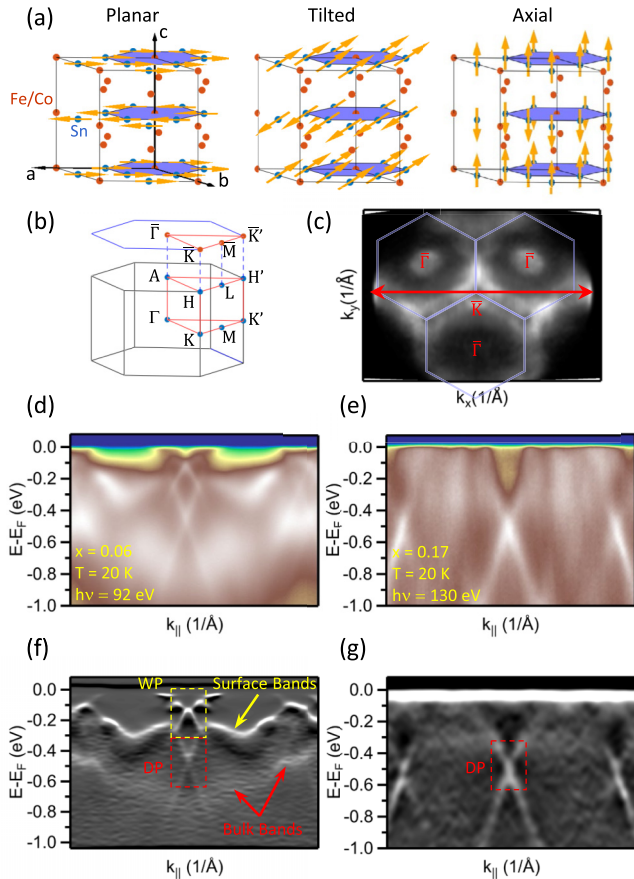


FIG. 1. Magnetic and electronic structure of $(\text{Fe}_{1-x}\text{Co}_x)\text{Sn}$. (a) Schematic of atomic and magnetic structure for the planar, tilted, and axial magnetic phases. The kagome lattice is highlighted in purple. (b) Brillouin zone (BZ) with surface projection and high-symmetry points identified. (c) Fermi surface map for $x = 0.06$ with (BZ) overlay. Red arrow indicates ARPES energy-momentum cut for subsequent data. (d) ARPES data for $x = 0.06$ at $h\nu = 92$ eV, chosen to maximize the Dirac and Weyl-like band intensities. (e) ARPES data for $x = 0.17$ at $h\nu = 130$ eV, which corresponds to the H and H' points where a maximum gap at the Dirac point is predicted. (f), (g) Curvature method plot for ARPES data in (d) and (e), respectively. Surface WP for $x = 0.06$ is outlined in yellow, and bulk DPs are outlined in red.

of neighboring FM kagome lattices. On the surface of FeSn, a Stark effect occurs for the topmost Fe_3Sn layer and lifts the degeneracy of the Weyl-like points and shifts the surface kagome layer Weyl-like band to $E - E_F \sim 0.25$ eV in energy. The breaking of the combined PT symmetry on the surface results in a massive surface Weyl-like band with a predicted small ~ 5 -meV gap [28–30].

The addition of Co into the FeSn system to create $(\text{Fe}_{1-x}\text{Co}_x)\text{Sn}$ results in a reorientation of the itinerant magnetic moments in the kagome layers [23]. While the moments within each layer maintain their FM alignment, increasing Co tilts the magnetic moments from a planar phase parallel to the kagome plane through a tilted phase with magnetic moments tilted out of the kagome plane to an axial phase with magnetic moments oriented along the c axis. Despite the reorientation of the magnetic moments in the kagome

planes, neighboring layers maintain their AFM arrangement as shown schematically in Fig. 1(a). For $x \sim 0.15$, the axial phase is the ground state of the system, but for $0 < x < 0.15$, a temperature-dependent second-order phase transition between the phases is observed [23]. Theoretical calculations have predicted that this spin reorientation to the axial phase should break the nonsymmorphic S_{2z} symmetry and open a large ~ 70 -meV gap at the H and H' Dirac points in the electronic dispersion [28].

Here angle-resolved photoemission spectroscopy (ARPES) combined with constrained magnetic moment first-principles calculations is used to investigate the evolution of the electronic structure of $(\text{Fe}_{1-x}\text{Co}_x)\text{Sn}$ with both composition and temperature. The bulk Dirac and surface Weyl-like bands are clearly observed with evidence for a gap at the bulk Dirac point in the low-temperature axial ground state, in agreement with theoretical calculations. However, no changes are observed in the experimental bulk Dirac dispersion, as the magnetic phase is tuned with temperature from planar through tilted to the axial magnetic phase, which disagrees with theoretical predictions. A distinct evolution of the surface Weyl-like bands compared to the bulk Dirac bands is observed, indicative of a reduction or disordering of the magnetic moment on the surface, which is likely due to sample aging of the cleaved bulk crystals. The shifting of the Weyl-like band energies combined with thermal broadening of the data could obscure the Dirac gap evolution with temperature, but the interplay between magnetism and topology is evident. Further experimental and theoretical investigation of the surface magnetism for the different surface terminations is required to fully understand the origins of the observed surface band evolution. Nonetheless, the dichotomy between surface and bulk behavior highlights the challenges in interrogating magnetic topological systems that can lead to contradicting results.

II. METHODS

Crystals of $(\text{Fe}_{1-x}\text{Co}_x)\text{Sn}$ were grown via the flux method, i.e., slow cooling a melt with a tin flux. The crystal structure, transport and magnetic properties were well characterized prior to the photoemission measurements as described elsewhere [23]. For these studies, $x = 0.06$ and 0.17 were used to investigate the temperature-dependent phases and axial ground state, respectively.

The ARPES measurements were conducted at Beamline 5-2 at the Stanford Synchrotron Radiation Lightsource utilizing a Scienta DA30L electron spectrometer and base pressure of better than 5×10^{-11} Torr. Linearly horizontal polarized light in the photon energy range $h\nu = 90 - 130$ eV was used for the measurements. The beamline has a nominal 0.04 mm² spot size, and a total energy resolution of ~ 16 meV was set for the measurements. Single crystals were mounted to sample posts using silver epoxy and cleaved in vacuum by knocking off a post mounted to the top of the sample.

To examine the dependence of the electronic band structure on magnetic ordering, we carry out density functional theory (DFT) calculations. Following the DFT work by Sales *et al.* [31], we use the Vienna *ab initio* simulation package (VASP) [32], which uses the projector augmented wave

method [33] with the generalized gradient approximation in the parametrization of Perdew, Burke, and Ernzerhof [34] for the exchange correlation. For Fe a standard potential is used (Fe in the VASP distribution), and for Sn a potential where the d states are treated as valence states, is used (Sn_d). We use the experimental structure doubled along the c -axis direction to account for the layered AFM ordering. In most cases, we use an $8 \times 8 \times 6$ k -point grid and an energy cutoff of 500 eV. The $+U$ correction is not included because FeSn is an itinerant magnetic system, but the spin-orbit coupling (SOC) is included to study the dependence of the electronic band structure on the direction as well as the size of ordered moments on Fe sites. For this purpose we carry out the constrained magnetism calculations by setting `I_CONSTRAINED_M = 2` and fixing the direction and the size of ordered moments.

III. RESULTS

The ARPES Fermi surface for $(\text{Fe}_{1-x}\text{Co}_x)\text{Sn}$ $x = 0.06$ is shown in Fig. 1(c) and is similar to previous reports [28]. Figures 1(d) and 1(e) show the low-temperature electronic structure for $x = 0.06$ and 0.17, respectively, through the \bar{K} point in a direction that is perpendicular to the $\Gamma - K$ direction. This cut orientation was chosen to maximize the appearance of the bulk Dirac and surface Weyl-like bands. The topological bands are clearly resolved in the raw data, but Figs. 1(f) and 1(g) show plots of a “1D curvature method” analysis, described in Ref. [35], highlighting the dispersive features [35]. The $(\text{Fe}_{1-x}\text{Co}_x)\text{Sn}$ system has a three-dimensional electronic dispersion, and different k_z are accessible by varying the photon energy. From previous reports, $h\nu = 130$ eV corresponds to the $k_z = \pi/c$, where the H and H' points occur [28]. Figure 1(e) shows the electronic structure at $h\nu = 130$ eV for $x = 0.17$ in the axial ground state. While the bulk Dirac bands are clearly visible in the data, photon energy-dependent matrix elements suppress the observation of the surface Weyl-like bands. However, by using $h\nu = 92$ eV, which corresponds to $k_z \sim 0.48\pi/c$, both the bulk Dirac bands and surface Weyl-like bands are clearly visible, as shown for $x = 0.06$ in Fig. 1(d). For $x = 0.06$ the bulk Dirac point (DP) and surface Weyl-like point (WP) are located at $E - E_F \sim -0.41$ eV and $E - E_F \sim -0.12$ eV, respectively, in agreement with previous measurements of undoped FeSn [28]. For $x = 0.17$ the WP intensity suppression prevents an accurate determination, but the DP is located further below the Fermi energy at $E - E_F \sim -0.5$ eV.

A. Axial ground state for $x = 0.17$

Theoretical band-structure calculations predict a large $2\Delta \sim 70$ meV gap to open at the bulk DP in the axial phase [28]. To understand the implications of the axial AFM phase on the electronic structure, a closer investigation of the Dirac bands highlighted in Fig. 1(g) are presented in Fig. 2. The curvature method analysis for the data in Fig. 1(g) around the vicinity of the DP, displayed in Fig. 2(j), shows evidence of a gapped electronic structure with $2\Delta \sim 70$ meV. However, since such features are hard to observe in the raw data, an in-depth investigation is performed to confirm the reliability of such an analysis.

Figure 2(a) shows the data in the vicinity of the DP that has been binned along the momentum axis to aid in the analysis. Plots of the energy spectra at constant momentum, i.e., energy distribution curves (EDCs), are presented for each bin in Fig. 2(d). Several features in the data and EDCs should be noted that can affect the analysis and our understanding of the existence, or not, of a gap at the DP.

From the data plotted in Fig. 1(e), as well as the plot of EDCs in Fig. 2(d), the intensity of the Dirac bands above the DP is markedly lower compared to the bands below the DP. Upon closer inspection, the intensity of the bands above and below the DP are similar away from the DP, as highlighted by the green curve in Fig. 2(d) and Fig. S2 in the Supplemental Material [36], and only the intensity of the bands above the DP are suppressed as the DP is approached, emphasized by the blue curve in Fig. 2(d) (see also Fig. S2 [36]). Previous reports have noted potential spin-selective matrix element effects in the vicinity of the Dirac bands that can alter band intensities [28,37], but the differences in behavior of the Dirac bands above and below the DP are unusual.

In addition to the intensity suppression of the bands above the DP, the spectral widths of the EDC features above and below the DP decrease as the DP is approached, as shown in Fig. S2 in the Supplemental Material [36]. As shown in Fig. 4, theory predicts several bands that converge at this DP that can affect both the intensity distribution and spectral widths of the observed band structure. Finally, the background intensity away from the dispersive features is lower above the DP when compared to below the Dirac point.

Fitting the entire spectra with two Lorentz functions plus a linear background fails to achieve reasonable results. However, when the FWHM for both Lorentz functions is constrained to the intermediate fitted values from the blue curve in Fig. 2(d) (see Fig. S2 [36]), then a gap of $2\Delta = 40 \pm 30$ meV results as shown in Fig. 2(g). It should be noted that the fitted dispersion deviates from a linear behavior, which could be due to the multiple bands with different dispersions in the region; see also the Supplemental Material [36]. While the analysis suggests a gapped structure, the empirical observations of variations of the intensity and width of the spectral features in the data raises questions regarding the validity of the gapped structure observed in Figs. 2(g) and 2(j).

To investigate how the observed variations in the spectral intensity, width and background can affect EDC fits and the curvature method analysis, a phenomenological model is developed to simulate ARPES data where similar analysis can be performed. Two overlapping bands with linear dispersion are assumed and modeled according to a simple interaction matrix [38,39],

$$\begin{vmatrix} \epsilon_1(k) & \Delta \\ \Delta & \epsilon_2(k) \end{vmatrix},$$

where $\epsilon_1(k)$ and $\epsilon_2(k)$ are the band energies and Δ is a momentum-independent interaction term. The spectral weight is computed and convoluted with a Lorentz function. To mimic the reduction of the dispersion widths observed in the data, the FWHM of the Lorentz function is reduced from 0.4 eV to 0.24 eV using a parabolic function with the minimum occurring at the DP. In addition, a similar parabolic function is used to reduce the intensity of the bands above

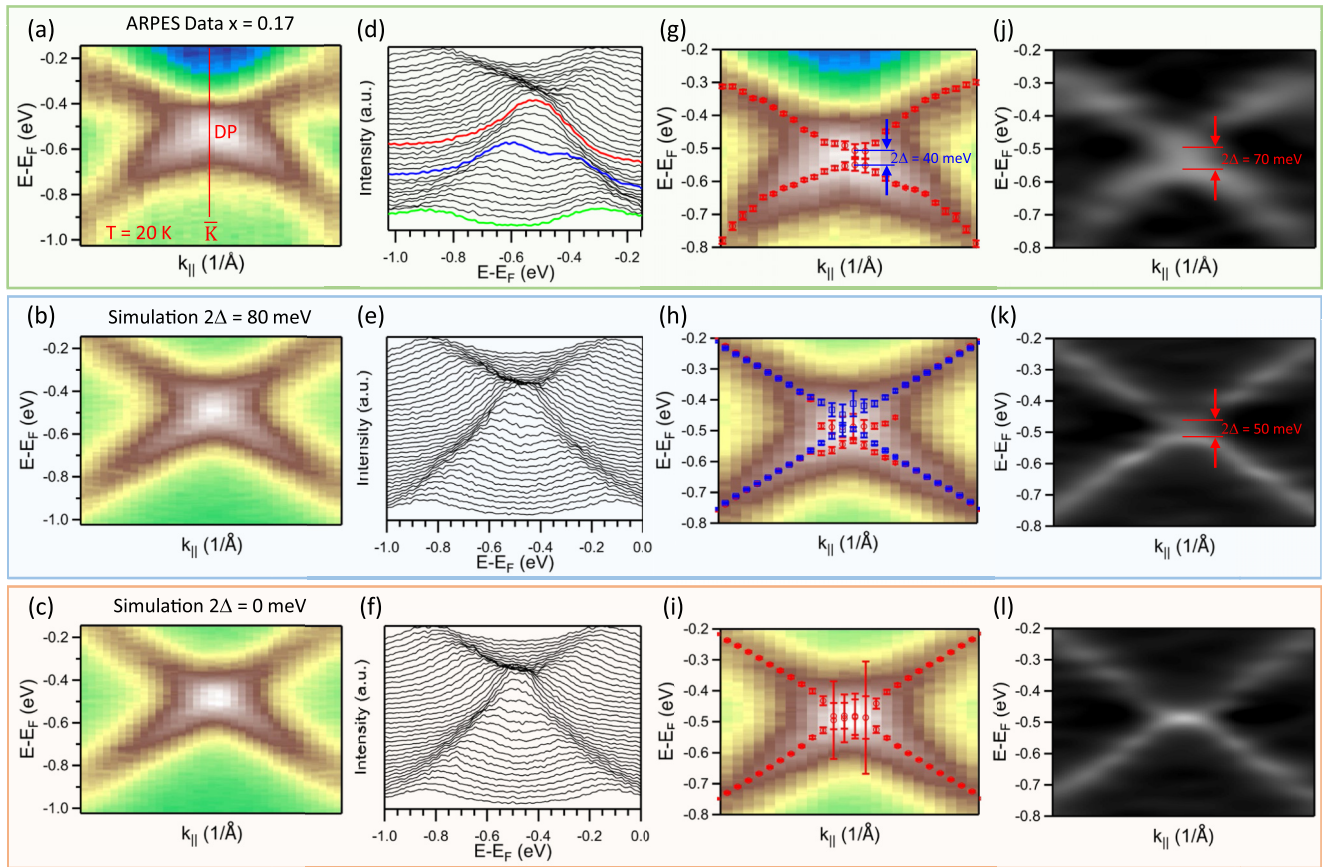


FIG. 2. Comparison of ARPES data for $x = 0.17$ in the low-temperature axial phase with simulations. (a–c) Image plots for region around the bulk DP outlined in Fig. 1(g) for binned ARPES data, $2\Delta = 80$ -meV simulation, and $2\Delta = 0$ -meV simulation, respectively. (d–f) EDC curves for binned ARPES data, $2\Delta = 80$ meV and $2\Delta = 0$ meV simulations, respectively. For the ARPES EDCs, the red, blue, and green curves highlight regions with different intensities and widths (see main text). (g–i) Fitted dispersion results for ARPES data, $2\Delta = 80$ meV, and $2\Delta = 0$ meV simulations, respectively. The blue markers are for free fit parameters, while the red markers are for constrained fits. (j–l) Curvature method analysis for ARPES data, $2\Delta = 80$ meV and $2\Delta = 0$ meV simulations, respectively.

the DP to 70% of their original value at the DP. These values are chosen based on trends observed in the ARPES data. Poisson noise is added to the resulting dispersing bands, which are then convoluted with a Gaussian with FWHM = 16 meV to match the energy resolution used for the ARPES measurements. Binned results for model data using $2\Delta = 80$ meV and 0 meV are plotted in Figs. 2(b) and 2(c), respectively. It should be emphasized that the $2\Delta = 80$ meV is manually implemented, which forces a gap in the model spectra and is chosen based on theoretical predictions. Simulating gapped and ungapped spectra with the atypical intensity and width behavior of the bands near the DP is designed to add credence to the gap analysis of the actual ARPES data.

The model data qualitatively follows the observed trends of the ARPES data and is used to help determine the reliability of the analysis performed on the data. Fitting the model data with $2\Delta = 80$ meV is shown in Fig. 2(h). If all parameters are free [blue markers in Fig. 2(h)], then a fitted gap of $2\Delta = 50 \pm 50$ meV results. If the widths of the two Lorentz functions are constrained during the fit, as was used for the actual data, then a gap of $2\Delta = 50 \pm 40$ meV results. The fitted gap is smaller than the $2\Delta = 80$ meV used to generate the simulated data. For simulations using $2\Delta = 0$ meV, the

fits must be constrained to prevent erratic results and confirms there is no gap in the structure.

The curvature method analysis for the simulated data yields a $2\Delta = 50$ meV gap for the gapped model as shown in Fig. 2(k), which again is smaller than the gap used to simulate the data. The reduction of both the intensity and width of the model functions in the simulations yields a suppression of the signal intensity in the curvature method plot, in agreement with the analysis on the ARPES data, but also leads to a reduction of the observed gap. The curvature method analysis of the simulated data with no gap confirms that no gap is observed in the analysis. These results add confidence to the evidence for a gapped structure in the ARPES data analysis. The model shows the reduction of intensity and widths observed in the ARPES data tends to reduce the measured gap, and thus the gap in the ARPES data may be larger than what is resolved. The combination of the analysis on the data as well as the simulations allow us to set a conservative gap estimate of $2\Delta \sim 60 - 80$ meV in the ARPES data due to the axial AFM magnetic structure.

Given the number of bands in the vicinity of the DP observed in theoretical calculation (see Fig. 4), a simple model with linear dispersions may not capture the needed complexities of the underlying band structure in the

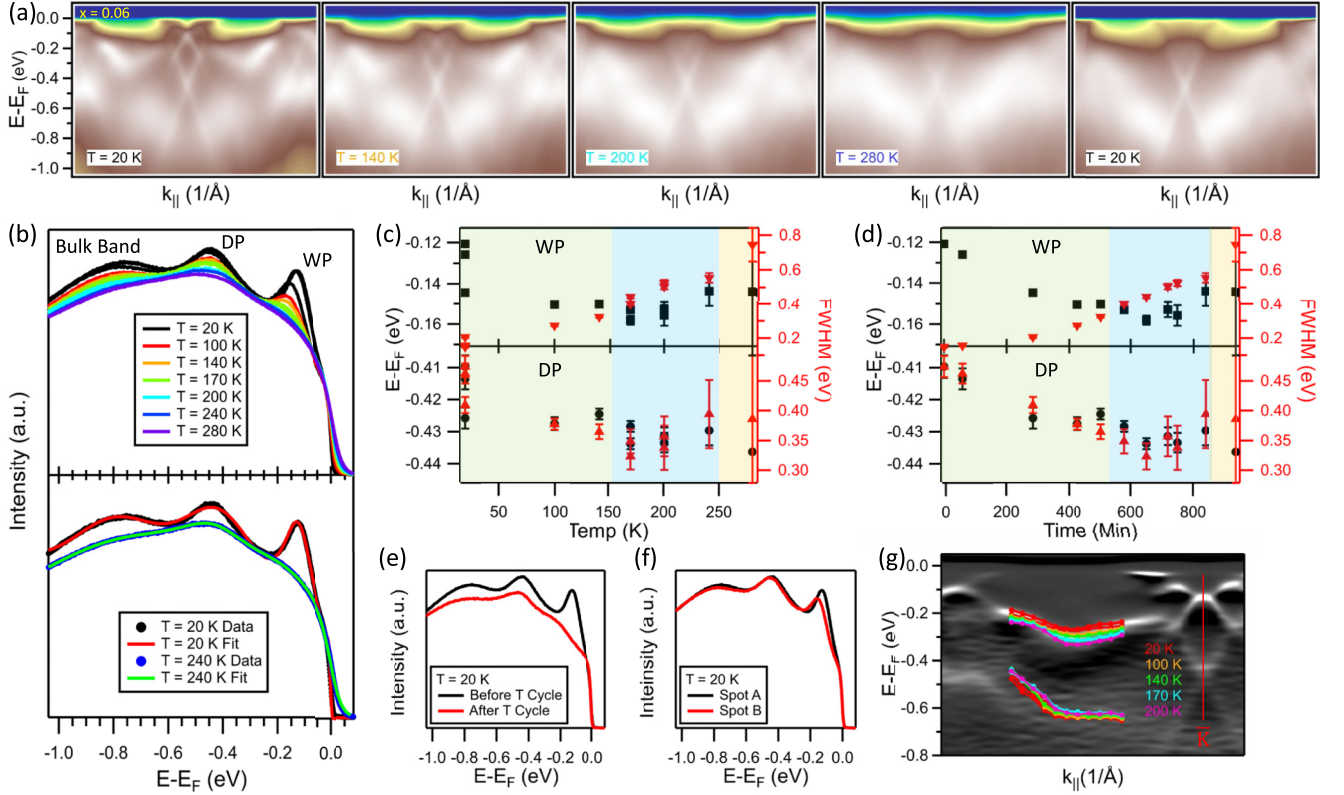


FIG. 3. Temperature-dependent ARPES data and EDC fits for $x = 0.06$. (a) ARPES data for $x = 0.06$ taken at different temperatures with the rightmost panel taken after cooling back down to $T = 20$ K. (b) EDCs at the \bar{K} point showing the surface WP, bulk DP, and bulk bands for the different temperatures. Model fits of the data are shown for $T = 20$ K and 240 K. (c) Model fit results vs temperature for the position and width of the surface WP and bulk DP. (d) Model fit results vs data collection time for the position and width of the surface WP and bulk DP. The planar (green), tilted (blue), and axial (orange) phases are shaded in (c) and (d). (e) Comparison of EDCs at $T = 20$ K before the temperature cycle and after the temperature cycle, highlighting the degradation of the surface WP spectral intensity. (f) Comparison of EDCs at $T = 20$ K before the temperature cycle for two different probed locations on the sample highlighting the sample surface inhomogeneities. (g) Curvature method plot of $x = 0.06$ ARPES data with temperature-dependent model fit results overlay for surface and bulk dispersive features away from the \bar{K} high-symmetry point.

simulations. In the Supplemental Material a similar analysis is performed using the theoretical bulk spectral function for the planar and axial phases as the starting point for simulating the ARPES data [36]. As shown in Fig. S7 [36], there are additional spectral features in the simulated data that are not observed in the ARPES data, which are likely due to photoemission matrix element effects. Nonetheless, the curvature method analysis shown in Fig. S7 still shows the existence of a gap in the axial phase.

Ideally, one would observe peak-dip-peak features in the EDC line profile across the DP to demonstrate a gapped electronic structure. However, as our simulations show, this expectation is not a necessary criterion for gap determination, as such features do not exist in our model where a gap is manually inserted. Bands that yield broad spectral features with energy widths comparable to the gap tend to hide this peak-dip-peak line profile and generate larger-than-desired fitting errors, but this does not necessarily translate into a nonexistent gap. By carefully modeling the spectral function of a simple model that reflects observed trends in the ARPES data we show that traditional EDC line fits and curvature method analysis tend to underestimate the actual size of the

energy gap. While the broad spectral features prevent a precise determination of the gap size, it does demonstrate the existence of a gap and allows us to estimate its size. As we have shown, accurately modeling the spectral function is a useful tool for benchmarking traditional ARPES analysis techniques and evaluating subtle details in the electronic structure of ARPES data.

Previous results show a temperature-dependent phase transition out of the axial AFM ground state at $T \sim 150$ K [23]. However, as shown in Supplemental Material Fig. S1 [36], thermal broadening prevents an accurate determination of the gap closing at elevated temperatures.

B. Temperature dependence for $x = 0.06$

For $x = 0.06$ the ground state is in the planar magnetic phase. Magnetization and neutron measurements show a transition to the axial phase at $T_2 = 256$ K and to the tilted phase at $T_1 = 155$ K [23]. To investigate the effects of the changing magnetic moments on the electronic structure, temperature-dependent data were taken as shown in Fig. 3. From the

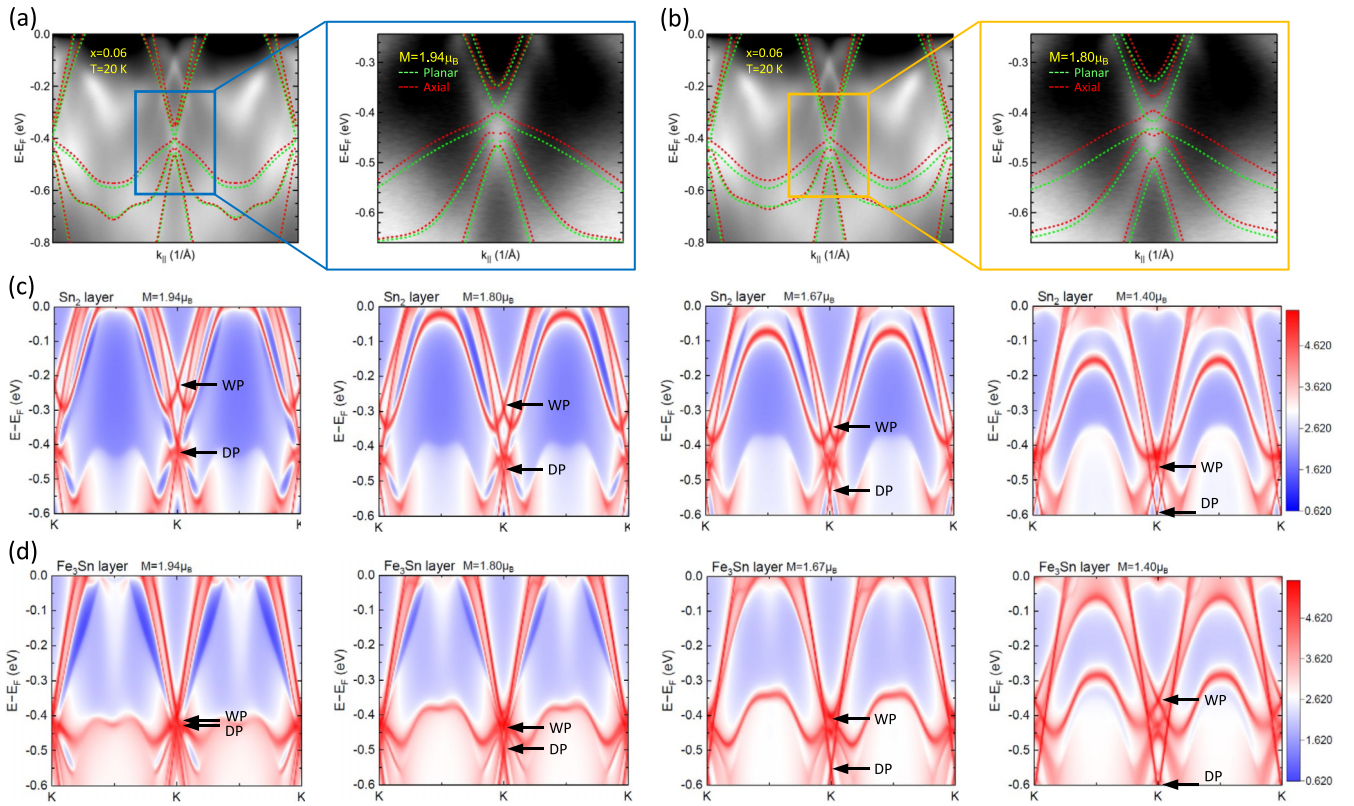


FIG. 4. Comparison of ARPES with DFT calculations. (a) DFT bulk bands with $M = 1.94 \mu_B$ for planar (green) and axial (red) AFM phases overlaid on ARPES data for $x = 0.06$. In the zoomed region outlined in blue, the contrast for the ARPES data is adjusted to highlight the Dirac dispersion. (b) DFT bulk bands with $M = 1.80 \mu_B$ for planar (green) and axial (red) AFM phases overlaid on ARPES data for $x = 0.06$. In the zoomed region outlined in orange, the contrast for the ARPES data is adjusted to highlight the Dirac dispersion. (c) DFT slab calculations with Sn_2 termination for different M . (d) DFT slab calculations with Fe_3Sn termination for different M . For (c) and (d) the surface WP and the bulk DP are highlighted for clarity.

plots of the raw data in Fig. 3(a), general trends can be observed for the topological band dispersions. Most notably is the downward shift in energy of the surface WP as well as the disappearance of the surface Weyl-like bands. The intensity of the bulk Dirac bands decreases with increasing temperature but recovers as temperature is lowered again to $T = 20$ K, while the surface Weyl-like band intensity does not recover when subsequently cooled. To track the behavior of the bulk DP and surface WP, the EDC data through the points were fitted with a simple phenomenological model involving Lorentz functions for the DP and WP as well as a Gaussian function for the bulk bands at $E - E_F \approx -0.8$ eV. A Shirley background and a Fermi cutoff is included to model the entire EDC as shown in Fig. 3(b) [40,41]. Fit results for different temperatures are shown in Fig. 3(c). While Figs. 3(a) and 3(b) reveal a downward shift of the surface WP, multiple data points taken at the same temperature show significant scatter within the EDC fit data for the surface WP energy in Fig. 3(c). Such data scatter results in the appearance of a near constant energy for the surface WP with an increasing width. The bulk DP shows a relatively constant energy and width as temperature is increased. While the increasing width of the surface WP is indicative of a gap opening, the disappearance of the surface Weyl-like bands decreases the reliability of these fitted widths. The bulk DP data again shows large

scatter with little evidence of a gap structure forming with the changing magnetic moment.

We found that a more revealing way to approach the analysis is to plot the trends versus time of the data collection as shown in Fig. 3(d). Here clear trends become more evident and reveal a monotonic decrease of the WP energy from $E - E_F \sim -0.12$ eV to $E - E_F \sim -0.16$ eV, a 33% shift in energy, with time along with a factor of 4 increase in the fit width of the feature. These trends, along with the disappearance of the surface Weyl-like bands, are indicative of sample aging. The bulk Dirac bands show a slight decrease in energy with temperature from $E - E_F \sim -0.41$ eV to $E - E_F \sim -0.43$ eV, a 5% shift in energy, with a large reduction in fit width. The reduction in width of the feature is opposite the trend expected for an opening gap. As shown in the bottom panel of Fig. 3(b), the width and position of the bulk DP feature are slightly skewed at low temperature due to using a simplistic model, but the fits of the bulk features improve as the surface feature disappears. Hence the trends in both the WP and DP width are attributed to the disappearance of the surface Weyl-like bands. The conclusion is that surface aging results in the disappearance of the surface Weyl-like bands. While no clear evidence of a gap is observed for the bulk Dirac bands, the combination of thermal broadening and shifting of the Weyl-like bands could obscure the gap opening.

While the data does not support the opening of a gap due to the reorientation of the magnetic moments, additional trends in the data are observed that give us insight into the band-structure evolution with temperature and/or time. In the low-temperature data shown in Fig. 3(a) and its curvature method plot in 3(g), additional bands are observed at around $E - E_F = -0.2$ to -0.3 eV between the \bar{K} points of neighboring Brillouin zones. Like the surface Weyl-like bands, these spectral features appear to move down in energy and disappear as the sample temperature increases. To better track the trends of these bands, EDCs at k_{\parallel} points away from the topological bands were fit with two Lorentz functions to mimic these shallow bands as well as deeper bands around $E - E_F \sim 0.6$ eV. The fit results are overlaid on the curvature method plot of the $T = 20$ K data in Fig. 3(g). As the sample temperature increases, the shallow bands move down in energy and follow the behavior of the surface Weyl-like bands, while the deeper bands do not move in energy with temperature. Due to the similarity in behavior with the surface Weyl-like bands, the shallow bands are attributed to surface states.

It should also be noted that surface inhomogeneities are observed in the ARPES data for different locations probed by the incoming light. The differences in the EDCs for the \bar{K} points at two different sample locations are shown in Fig. 3(f). There are subtle differences in the bulk DP and deeper bulk bands, but differences in the energy and intensity of the surface WP are more prominent at the different locations. In general, inhomogeneities in the surface Weyl-like bands are observed across the cleaved sample surface, while the bulk bands remain consistent. Since this is a metallic system, it is unlikely the variations of the Weyl-like band energies are related to variations in surface charge doping. Due to the ~ 0.04 -mm² spot size, a single sample spot was isolated for temperature-dependent data to ensure variations observed in the bands are due to temperature and not due to surface inhomogeneities.

C. Comparison with theory

To gain a deeper understanding of the observed band-structure evolution, DFT calculations, including spin-orbit coupling, are compared with the ARPES data as shown in Fig. 4 as well as in the Supplemental Material [36]. While the photon energy, $h\nu = 92$ eV, maximizes the intensity within the topological bands, it lies between the H and K points at $k_z \sim 0.48\pi/c$. Nonetheless, theoretical calculations reveal a gap opening at this k_z as the spins reorient along into the axial phase, in agreement with previous reports [28]. To understand the implications of spin reorientation and the size of the magnetic moment in the planar and axial phases, constrained magnetic calculations were performed as shown in Fig. 4(a) and in the Supplemental Material [36]. Previous reports indicate magnetic moments in the first and bulk Fe₃Sn layers to be $2.16 \mu_B$ and $1.96 \mu_B$, respectively [28]. There is a large shift of the bulk bands for different magnetic moments as shown in Fig. S3 in the Supplemental Material [36], but the theory best matches the ARPES data for $M \geq 1.8 \mu_B$. For the larger magnetic moments, the bulk axial and planar band dispersions are similar, with the largest difference occurring

at the DP as shown in Figs. 4(a) and 4(b), which agrees with the low-temperature ARPES data for $x = 0.06$ in the planar phase. No shifting or renormalization of the theoretical bands is necessary to match the ARPES data, indicative of a lack of strong electronic correlations in the system. This is to be expected for an itinerant magnetic metallic system and confirms the DFT approach without a Coulomb interaction potential ($+U$) accurately represents the system.

Here we briefly comment on the relative stability between the axial and planar phases. With the large ordered moment, $M \sim 1.94 \mu_B$, the DFT total energy of the planar state is -12.4018 eV per formula unit and that of the axial state is -12.3992 eV per formula unit. Thus the former is more stable than the latter by 2.6 meV. With reducing the ordered moment, the relative energy reduces very rapidly and becomes smaller than 0.5 meV for $M < 1.8 \mu_B$. This indicates that the transition from the planar state to the axial state can be easily induced by increasing temperature or Co substitution, as experimentally observed.

The bulk band calculations do not reveal the Weyl-like bands at $E - E_F \sim -0.1$ eV at the \bar{K} point or bands at $E - E_F \sim -0.2$ eV away from \bar{K} point, implying that these are surface bands induced by the surface Stark effect [28]. To better understand the surface-induced bands and their relation to the observed ARPES data, spectral weight from theoretical slab calculations were determined for different magnetic moments in both the planar and axial phases, as shown in Figs. 4(c) and 4(d) and in the Supplemental Material [36]. There are two possible surface terminations, Sn₂ and Fe₃Sn, and slab calculations are presented for both. For the larger $M \geq 1.8 \mu_B$, as previously reported [28], only the Sn₂-terminated surface yields an observable surface WP shifted up in energy ~ 0.2 eV from the bulk DP. The Sn₂ slab calculations for $M = 1.94 \mu_B$ show the surface WP at $E - E_F = 0.24$ eV and are similar to the observed WP at $E - E_F = 0.12$ eV in the low-temperature $x = 0.06$ ARPES data. Interestingly, the slab calculations for the Sn₂ and Fe₃Sn layers show distinct trends in the position of the surface bands as the magnetic moment is varied. For the Sn₂ surface, the surface WP moves down in energy ~ 0.2 eV as the magnetic moment is reduced from $M = 1.94 \mu_B$ to $M = 1.4 \mu_B$, as shown in Fig. 4(c). This downward shift in energy with reduced magnetic moment continues for lower M , as shown in the Supplemental Material [36]. In contrast, the Fe₃Sn surface shows the opposite trends, where the surface WP is nearly degenerate in energy with the bulk DP for $M = 1.94 \mu_B$ and moves upwards in energy ~ 0.1 eV as the magnetic moment is reduced to $M = 1.4 \mu_B$, as shown in Fig. 4(d). Similarly, this trend continues for lower magnetic moments as shown in the Supplemental Material [36]. Since the Fe d states are more concentrated near the Fermi level compared to the extended Sn p states in energy [28], it is speculated that a possible anticrossinglike effect could create the dichotomy in behavior for the two surfaces. However, more efforts are required to confirm such behavior. Both surface terminations show similar trends in the low-energy spectral weight in the region between the \bar{K} points, with a downward shift from the Fermi level to $E - E_F \sim 0.1$ – 0.15 eV as the magnetic moment is reduced from $M = 1.94 \mu_B$ to $M = 1.4 \mu_B$, as shown in Figs. 4(c) and 4(d).

IV. DISCUSSION

The topological band structures for the bulk Dirac and surface Weyl-like bands are clearly visible in the ARPES data and are similar to previously published results [28]. Theoretical investigations have predicted that a large $2\Delta \sim 70$ -meV gap should open at the bulk DP with a reorientation of the magnetic moment out of the kagome lattice plane due to the breaking of the nonsymmorphic S_{2z} symmetry [28]. Previous transport and neutron investigations show the magnetic moment in the $(\text{Fe}_{1-x}\text{Co}_x)\text{Sn}$ material family can be tuned with composition and temperature [23]. Evidence for a gap is observed in the low-temperature axial phase for $x = 0.17$, but no clear changes to the bulk Dirac bands are observed as the magnetic moments reorient from the planar through the tilted to the axial phase in $x = 0.06$ with increasing temperature. The widths of the spectral features plus finite energy resolution and thermal broadening of the ARPES measurements may prevent the observation of gap features in the temperature-dependent data. Nonetheless, a large ~ 70 -meV gap is within the experimental resolution of the current measurements, and no signatures of such a gap formation are observed for $x = 0.06$ as the system temperature increases through the magnetic phase boundaries.

Differences are observed in the behavior of the surface Weyl-like bands compared to the bulk Dirac bands as the sample temperature increases. The disappearance of the surface bands with temperature and the reduction of the Dirac band intensity after temperature cycling is indicative of surface aging, but the downward energy shift of the surface bands only is unusual. Changes in carrier doping due to aging can alter observed band energies, but since all the bands do show aging effects, it is expected that all the observed band energies would be affected and not just the surface bands.

Theoretical calculations not only confirm a large gap should appear due to the breaking of S_{2z} symmetry but also reveal a large energy shift of the bulk bands away from the K point as the c -axis magnetic moment changes, which is not observed in the ARPES data. Contrary to bulk band behavior in the ARPES data, where a modest 5% energy shift is observed, the surface bands shift downwards 33% in energy as the temperature and/or time of measurement increases. Theoretical slab calculations for the Sn_2 termination agree with the ARPES data in the energy of the surface WP and also show a trend downward in energy as the magnetic moment is reduced.

In addition to the temperature trends in the surface bands, variations in the surface WP are observed due to surface inhomogeneities across the sample surface. For FeSn the magnetic anisotropy energy is shown to be small, on the order of 0.03 meV/unit cell, where small perturbations can manipulate the spin orientation [28,42,43]. This anisotropy contributes to the tunability of the magnetic moments but can also contribute to large magnetic inhomogeneities due to different terminations and defects on the surface. The spatial variations of the surface Weyl-like bands are likely due to inhomogeneities of the magnetic moments on the surface, resulting in variations of the observed band energies.

Similarly, shifts in energy as the sample surface ages are likely due to a reduction or disordering of the magnetic

moments due to surface aging effects. Our calculations show the energy difference between the planar and axial phases dramatically reduces with a small reduction of the magnetic moment, indicating a subtle reduction of M due to aging effects could easily lead to magnetic disorder. The differences in the surface potential which result in the appearance of the surface Weyl-like bands also result in alterations of the magnetic moments of the surface most Fe_3Sn layer being isolated to the surface Weyl-like bands and not affecting the bulk Dirac bands. Hence the observed behavior of the surface Weyl-like bands with temperature/time and variations in sample position suggest the magnetic moments in the surface most Fe_3Sn layer reorient or relax during the ARPES measurements. However, surface magnetic measurements are necessary to confirm the magnetic moments on the surface, as well as any disordering or relaxation over time.

In conclusion, evidence for a sizable $2\Delta \sim 60 - 80$ meV gap at the bulk DP is observed in the low-temperature axial phase for $x = 0.17$, but no clear gap opening is observed with temperature across the planar-to-axial phase transition in the $x = 0.06$ samples. However, large energy shifts of the surface bands are observed. The shift, and eventual disappearance, of the surface bands are attributed to a reduction and disordering of the surface magnetic moment as the sample ages after cleaving, which is an unavoidable artifact of the surface-sensitive experimental technique. The combination of thermal broadening and shifting of the surface Weyl-like bands could obscure the gap evolution with temperature, and more systematic studies at different doping levels are required to reveal the subtle details. The conflicting gap results for the two dopings are on par with investigations of other similar magnetic topological systems and highlight the challenges in disentangling magnetic and topological features in these material systems. Nonetheless, the shifting surface Weyl-like bands reveal the need to carefully track and account for subtle changes in surface magnetic moments during measurements. Such accounting is critical to understand their influence on surface-sensitive probes and could account for discrepancies observed in published results for related systems. Future efforts are necessary to understand the evolution of the surface magnetism, but clear links between the topological electronic structure and magnetic moment are evident, as our work has revealed.

The DOE will provide public access to these results of federally sponsored research in accordance with the DOE Public Access Plan [44].

ACKNOWLEDGMENTS

The work of all coauthors was supported by the U.S. Department of Energy, Office of Science, Basic Energy Sciences, Materials Sciences and Engineering Division. The use of the Stanford Synchrotron Radiation Lightsource, SLAC National Accelerator Laboratory, is supported by the U.S. Department of Energy, Office of Science, Office of Basic Energy Sciences, under Contract No. DE-AC02-76SF00515. This research used resources of the Compute and Data Environment for Science (CADES) at the Oak Ridge National Laboratory, which

is supported by the Office of Science of the U.S. Department of Energy under Contract No. DE-AC05-00OR22725. This manuscript has been authored in part by UT-Battelle, LLC, under Contract No. DE-AC05-00OR22725 with the U.S. Department of Energy (DOE). The U.S. government

retains and the publisher, by accepting the article for publication, acknowledges that the U.S. government retains a nonexclusive, paid-up, irrevocable, worldwide license to publish or reproduce the published form of this manuscript, or allow others to do so, for U.S. government purposes.

- [1] J. E. Moore, The birth of topological insulators, *Nature (London)* **464**, 194 (2010).
- [2] M. Z. Hasan and C. L. Kane, Colloquium: Topological insulators, *Rev. Mod. Phys.* **82**, 3045 (2010).
- [3] B. Yan and C. Felser, Topological materials: Weyl semimetals, *Annu. Rev. Condens. Matter Phys.* **8**, 337 (2017).
- [4] N. P. Armitage, E. J. Mele, and A. Vishwanath, Weyl and Dirac semimetals in three-dimensional solids, *Rev. Mod. Phys.* **90**, 015001 (2018).
- [5] C. Z. Chang, J. Zhang, X. Feng, J. Shen, Z. Zhang, M. Guo, K. Li, Y. Ou, P. Wei, L. L. Wang, Z. Q. Ji, Y. Feng, S. Ji, X. Chen, J. Jia, X. Dai, Z. Fang, S. C. Zhang, K. He, Y. Wang *et al.*, Experimental observation of the quantum anomalous Hall effect in a magnetic topological insulator, *Science* **340**, 167 (2013).
- [6] C. Liu, Y. Wang, H. Li, Y. Wu, Y. Li, J. Li, K. He, Y. Xu, J. Zhang, and Y. Wang, Robust axion insulator and Chern insulator phases in a two-dimensional antiferromagnetic topological insulator, *Nat. Mater.* **19**, 522 (2020).
- [7] R. S. K. Mong, A. M. Essin, and J. E. Moore, Antiferromagnetic topological insulators, *Phys. Rev. B* **81**, 245209 (2010).
- [8] M. Hirschberger, S. Kushwaha, Z. Wang, Q. Gibson, S. Liang, C. A. Belvin, B. A. Bernevig, R. J. Cava, and N. P. Ong, The chiral anomaly and thermopower of Weyl fermions in the half-Heusler GdPtBi, *Nat. Mater.* **15**, 1161 (2016).
- [9] M. M. Hosen, G. Dhakal, K. Dimitri, P. Maldonado, A. Aperis, F. Kabir, C. Sims, P. Riseborough, P. M. Oppeneer, D. Kaczorowski, T. Durakiewicz, and M. Neupane, Discovery of topological nodal-line fermionic phase in a magnetic material GdSbTe, *Sci. Rep.* **8**, 13283 (2018).
- [10] H. Li, S.-Y. Gao, S.-F. Duan, Y.-F. Xu, K.-J. Zhu, S.-J. Tian, J.-C. Gao, W.-H. Fan, Z.-C. Rao, J.-R. Huang, J.-J. Li, D.-Y. Yan, Z.-T. Liu, W.-L. Liu, Y.-B. Huang, Y.-L. Li, Y. Liu, G.-B. Zhang, P. Zhang, T. Kondo *et al.*, Dirac Surface States in Intrinsic Magnetic Topological Insulators EuSn_2As_2 and $\text{MnBi}_{2n}\text{Te}_{3n+1}$, *Phys. Rev. X* **9**, 041039 (2019).
- [11] M. M. Otrokov, I. Klimovskikh, H. Bentmann, D. Estyunin, A. Zeugner, Z. S. Aliev, S. Gass, A. U. B. Wolter, A. V. Koroleva, A. M. Shikin, M. Blanco-Rey, M. Hoffmann, I. P. Rusinov, A. Y. Vyazovskaya, S. V. Eremeev, Y. M. Koroteev, V. M. Kuznetsov, F. Freyse, J. Sanchez-Barriga, I. R. Amiraslanov *et al.*, Prediction and observation of an antiferromagnetic topological insulator, *Nature (London)* **576**, 416 (2019).
- [12] Y. J. Chen, L. X. Xu, J. H. Li, Y. W. Li, H. Y. Wang, C. F. Zhang, H. Li, Y. Wu, A. J. Liang, C. Chen, S. W. Jung, C. Cacho, Y. H. Mao, S. Liu, M. X. Wang, Y. F. Guo, Y. Xu, Z. K. Liu, L. X. Yang, and Y. L. Chen, Topological Electronic Structure and Its Temperature Evolution in Antiferromagnetic Topological Insulator MnBi_2Te_4 , *Phys. Rev. X* **9**, 041040 (2019).
- [13] Y.-J. Hao, P. Liu, Y. Feng, X.-M. Ma, E. F. Schwier, M. Arita, S. Kumar, C. Hu, R. Lu, M. Zeng, Y. Wang, Z. Hao, H.-Y. Sun, K. Zhang, J. Mei, N. Ni, L. Wu, K. Shimada, C. Chen, Q. Liu *et al.*, Gapless Surface Dirac Cone in Antiferromagnetic Topological Insulator MnBi_2Te_4 , *Phys. Rev. X* **9**, 041038 (2019).
- [14] R. C. Vidal, H. Bentmann, T. R. F. Peixoto, A. Zeugner, S. Moser, C. H. Min, S. Schatz, K. Kißner, M. Unzelmann, C. I. Fornari, H. B. Vasili, M. Valvidares, K. Sakamoto, D. Mondal, J. Fujii, I. Vobornik, S. Jung, C. Cacho, T. K. Kim, R. J. Koch *et al.*, Surface states and Rashba-type spin polarization in antiferromagnetic MnBi_2Te_4 (0001), *Phys. Rev. B* **100**, 121104(R) (2019).
- [15] S. H. Lee, Y. Zhu, Y. Wang, L. Miao, T. Pillsbury, H. Yi, S. Kempinger, J. Hu, C. A. Heikes, P. Quarterman, W. Ratcliff, J. A. Borchers, H. Zhang, X. Ke, D. Graf, N. Alem, C.-Z. Chang, N. Samarth, and Z. Mao, Spin scattering and non-collinear spin structure-induced intrinsic anomalous Hall effect in antiferromagnetic topological insulator MnBi_2Te_4 , *Phys. Rev. Res.* **1**, 012011(R) (2019).
- [16] D. Nevola, H. X. Li, J. Q. Yan, R. G. Moore, H. N. Lee, H. Miao, and P. D. Johnson, Coexistence of Surface Ferromagnetism and a Gapless Topological State in MnBi_2Te_4 , *Phys. Rev. Lett.* **125**, 117205 (2020).
- [17] W. Ko, M. Kolmer, J. Yan, A. D. Pham, M. Fu, F. Lüüpke, S. Okamoto, Z. Gai, P. Ganesh, and A.-P. Li, Realizing gapped surface states in the magnetic topological insulator $\text{MnBi}_{2-x}\text{Sb}_x\text{Te}_4$, *Phys. Rev. B* **102**, 115402 (2020).
- [18] Z. Lin, J. H. Choi, Q. Zhang, W. Qin, S. Yi, P. Wang, L. Li, Y. Wang, H. Zhang, Z. Sun, L. Wei, S. Zhang, T. Guo, Q. Lu, J. H. Cho, C. Zeng, and Z. Zhang, Flatbands and Emergent Ferromagnetic Ordering in Fe_3Sn_2 Kagome Lattices, *Phys. Rev. Lett.* **121**, 096401 (2018).
- [19] L. Ye, M. Kang, J. Liu, F. von Cube, C. R. Wicker, T. Suzuki, C. Jozwiak, A. Bostwick, E. Rotenberg, D. C. Bell, L. Fu, R. Comin, and J. G. Checkelsky, Massive Dirac fermions in a ferromagnetic kagome metal, *Nature (London)* **555**, 638 (2018).
- [20] E. Liu, Y. Sun, N. Kumar, L. Muchler, A. Sun, L. Jiao, S. Y. Yang, D. Liu, A. Liang, Q. Xu, J. Kroder, V. Suss, H. Borrmann, C. Shekhar, Z. Wang, C. Xi, W. Wang, W. Schnelle, S. Wirth, Y. Chen *et al.*, Giant anomalous Hall effect in a ferromagnetic kagome-lattice semimetal, *Nat. Phys.* **14**, 1125 (2018).
- [21] K. Kuroda, T. Tomita, M. T. Suzuki, C. Bareille, A. A. Nugroho, P. Goswami, M. Ochi, M. Ikhlas, M. Nakayama, S. Akebi, R. Noguchi, R. Ishii, N. Inami, K. Ono, H. Kumigashira, A. Varykhalov, T. Muro, T. Koretsune, R. Arita, S. Shin *et al.*, Evidence for magnetic Weyl fermions in a correlated metal, *Nat. Mater.* **16**, 1090 (2017).
- [22] W. R. Meier, M.-H. Du, S. Okamoto, N. Mohanta, A. F. May, M. A. McGuire, C. A. Bridges, G. D. Samolyuk, and B. C. Sales, Flat bands in the CoSn-type compounds, *Phys. Rev. B* **102**, 075148 (2020).
- [23] W. R. Meier, J. Yan, M. A. McGuire, X. Wang, A. D. Christianson, and B. C. Sales, Reorientation of antiferromagnetism in cobalt doped FeSn, *Phys. Rev. B* **100**, 184421 (2019).

- [24] C. Djega-Mariadassou, P. Lecocq, and A. Michale, Etude magnétique et structurale des phases MSn_2 et MSn ($M = Fe, Co$) et des solutions solides $(Fe_xM_{1-x})Sn$, $(Fe_xM_{1-x})Sn_2$ ($M = Co, Ni$), *Ann. Chimie* **4**, 175 (1969).
- [25] L. Häggström, T. Ericsson, R. Wäppling, and K. Chandra, Studies of the magnetic structure of $FeSn$ using the Mössbauer effect, *Phys. Scr.* **11**, 47 (1975).
- [26] K. Yamaguchi and H. Watanabe, Neutron diffraction study of $FeSn$, *J. Phys. Soc. Jpn.* **22**, 1210 (1967).
- [27] S. K. Kulshreshtha and P. Raj, Anisotropic hyperfine fields in $FeSn$ by Mossbauer spectroscopy, *J. Phys. F: Met. Phys.* **11**, 281 (1981).
- [28] Z. Lin, C. Wang, P. Wang, S. Yi, L. Li, Q. Zhang, Y. Wang, Z. Wang, H. Huang, Y. Sun, Y. Huang, D. Shen, D. Feng, Z. Sun, J.-H. Cho, C. Zeng, and Z. Zhang, Dirac fermions in antiferromagnetic $FeSn$ kagome lattices with combined space inversion and time-reversal symmetry, *Phys. Rev. B* **102**, 155103 (2020).
- [29] J.-Y. You, C. Chen, Z. Zhang, X.-L. Sheng, S. A. Yang, and G. Su, Two-dimensional Weyl half-semimetal and tunable quantum anomalous Hall effect, *Phys. Rev. B* **100**, 064408 (2019).
- [30] W. Wu, Y. Jiao, S. Li, X.-L. Sheng, Z.-M. Yu, and S. A. Yang, Hourglass Weyl loops in two dimensions: Theory and material realization in monolayer $GaTeI$ family, *Phys. Rev. Mater.* **3**, 054203 (2019).
- [31] B. C. Sales, J. Yan, W. R. Meier, A. D. Christianson, S. Okamoto, and M. A. McGuire, Electronic, magnetic, and thermodynamic properties of the kagome layer compound $FeSn$, *Phys. Rev. Mater.* **3**, 114203 (2019).
- [32] G. Kresse and J. Furthmüller, Efficient iterative schemes for *ab initio* total-energy calculations using a plane-wave basis set, *Phys. Rev. B* **54**, 11169 (1996).
- [33] G. Kresse and D. Joubert, From ultrasoft pseudopotentials to the projector augmented-wave method, *Phys. Rev. B* **59**, 1758 (1999).
- [34] J. P. Perdew, K. Burke, and M. Ernzerhof, Generalized Gradient Approximation Made Simple, *Phys. Rev. Lett.* **77**, 3865 (1996).
- [35] P. Zhang, P. Richard, T. Qian, Y. M. Xu, X. Dai, and H. Ding, A precise method for visualizing dispersive features in image plots, *Rev. Sci. Instrum.* **82**, 043712 (2011).
- [36] See Supplemental Material at <http://link.aps.org/supplemental/10.1103/PhysRevB.106.115141> for $x = 0.17$ temperature-dependent ARPES data, Lorentz fits of bands near the Dirac point for $x = 0.17$, DFT band-structure overlay on ARPES data for different magnetic moments, spectral weight slab calculations with different magnetic moments for bulk plus Fe_3Sn , and Sn_2 surface terminations, and gap analysis using ARPES simulations from bulk DFT spectral function calculations.
- [37] M. Kang, L. Ye, S. Fang, J. S. You, A. Levitan, M. Han, J. I. Facio, C. Jozwiak, A. Bostwick, E. Rotenberg, M. K. Chan, R. D. McDonald, D. Graf, K. Kaznatcheev, E. Vescovo, D. C. Bell, E. Kaxiras, J. van den Brink, M. Richter, M. Prasad Ghimire *et al.*, Dirac fermions and flat bands in the ideal kagome metal $FeSn$, *Nat. Mater.* **19**, 163 (2020).
- [38] V. Brouet, W. L. Yang, X. J. Zhou, Z. Hussain, R. G. Moore, R. He, D. H. Lu, Z. X. Shen, J. Laverock, S. B. Dugdale, N. Ru, and I. R. Fisher, Angle-resolved photoemission study of the evolution of band structure and charge density wave properties in, *Phys. Rev. B* **77**, 235104 (2008).
- [39] R. G. Moore, V. Brouet, R. He, D. H. Lu, N. Ru, J. H. Chu, I. R. Fisher, and Z. X. Shen, Fermi surface evolution across multiple charge density wave transitions in $ErTe_3$, *Phys. Rev. B* **81**, 073102 (2010).
- [40] D. A. Shirley, High-resolution x-ray photoemission spectrum of the valence bands of gold, *Phys. Rev. B* **5**, 4709 (1972).
- [41] J. E. Castle and A. M. Salvi, Interpretation of the Shirley background in x-ray photoelectron spectroscopy analysis, *J. Vac. Sci. Technol. A* **19**, 1170 (2001).
- [42] L. Šmejkal, J. Zelezny, J. Sinova, and T. Jungwirth, Electric Control of Dirac Quasiparticles by Spin-Orbit Torque in an Antiferromagnet, *Phys. Rev. Lett.* **118**, 106402 (2017).
- [43] L. Šmejkal, Y. Mokrousov, B. Yan, and A. H. MacDonald, Topological antiferromagnetic spintronics, *Nat. Phys.* **14**, 242 (2018).
- [44] <http://energy.gov/downloads/doe-public-access-plan>.